Microchemical Journal 170 (2021) 106643

Contents lists available at ScienceDirect

Microchemical Journal

journal homepage: www.elsevier.com/locate/microc

Carbohydrate antigen 19-9 electrochemical immunosensor based on 1D-MoS_2 nanorods/$LiNb_3O_8$ and polyoxometalate-incorporated gold nanoparticles

Mehmet Lütfi Yola [a,*], Necip Atar [b]

[a] Hasan Kalyoncu University, Faculty of Health Sciences, Department of Nutrition and Dietetics, Gaziantep, Turkey
[b] Pamukkale University, Faculty of Engineering, Department of Chemical Engineering, Denizli, Turkey

ARTICLE INFO

Keywords:
Carbohydrate antigen 19-9
1D-MoS_2 nanorods
Polyoxometalate
Immunosensor

ABSTRACT

The diagnosis of disease and the monitoring of patient in cancer research are related to biomarkers. Carbohydrate antigen 19-9 (CA 19-9) as the main tumor biomarker is necessary for digestive tract associated cancers. In this study, 1D-MoS_2 nanorods/$LiNb_3O_8$ (1D-MoS_2 NRs/LNO) as signal amplification and polyoxometalate-incorporated gold nanoparticles (AuNPs@POM) as sensor platform were prepared and the electrochemical immunosensor application was conducted based on 1D-MoS_2 NRs/LNO and AuNPs@POM for CA 19-9 detection. After the preparation of AuNPs@POM nanocomposite, primer antibody immobilization was conducted via amino-gold affinity between primer antibody and AuNPs@POM nanocomposite. After that, strong π-π and electrostatic interactions between seconder antibody and 1D-MoS_2 NRs/LNO provided the successful conjugation of seconder antibody. The physicochemical characterizations including scanning electron microscopy (SEM), transmission electron microscopy (TEM), x-ray photoelectron spectroscopy (XPS), x-ray diffraction (XRD) were performed for electrochemical CA 19-9 immunosensor. Furhermore, to asses the electrochemical performance of the immunosensor, cyclic voltammetry (CV), differential pulse voltammetry (DPV) and electrochemical impedance spectrospcopy (EIS) techniques were performed. The quantification limit (LOQ) and the detection limit (LOD) values were obtained as 0.10 μU mL^{-1} and 0.030 μU mL^{-1}, respectively. This immunosensor having high selectivity, stability and reusability creates a novel chance for clinical immunoassays.

1. Introduction

CA 19-9 was found using monoclonal antibody against human colorectal carcinoma cell line as a tumor-associated carbohydrate antigen [1]. It is widely accepted as a useful tumor marker in the diagnosis and treatment of cancer patients. This antigen has a carbohydrate structure as a sialyl derivative of Lacto-N-fucopentaose II, which is the hapten of human blood group Lewis antigen. This antigen is found in small amounts in human epithelium [2]. However, this antigen is produced more and begins to appear in blood and secretions with the formation of carcinoma. CA 19-9 is usually found in the serum of patients with gastrointestinal carcinoma. Especially, it is seen in pancreatic and biliary tract carcinomas. It is frequently shown in many adenocarcinoma tissues in immunohistochemical studies. Although it is known that there may be an increase in CA 19-9 level in benign diseases, values higher than 1000 U mL^{-1} are indicative of a 99% malignant condition [3]. CA 19-9's existence is known in normal kidney, renal tubules and pelvic mucosa. In addition, it is reported that its level increases in patients with pancreatic cancer. Thereby, CA 19-9's selective determination in low levels can be favorable to clinical diagnoses in patients. Up to now, several methods have been presented for the determination of CA 19-9 such as chromatography and photoelectrochemical immunoassays [4]. However, these techniques are not useful owing to the time-consuming sample preparation procedures.

Early diagnosis of cancer increases the chance of treatment. Today, many types of cancer can be diagnosed after the whole body has metastasized. There is an urgent diagnosis method need for cancer determination. Biosensor technology plays an important role at this point. They are devices designed to identify a specific biological analyte/biomarker and convert it into a signal that can be analyzed [5-10]. Immunosensors, which are a kind of biosensor, are produced by immobilizing antigens or antibodies to the sensor surface. Direct

* Corresponding author.
E-mail address: mlutfi.yola@hku.edu.tr (M.L. Yola).

https://doi.org/10.1016/j.microc.2021.106643
Received 11 May 2021; Received in revised form 9 July 2021; Accepted 12 July 2021
Available online 14 July 2021

immunosensors are designed to generate an antibody-antigen complex that causes physical change in signal. Electrodes, membranes, piezoelectric materials or optically active surface materials are sufficiently sensitive for direct immunosensor construction [10,11]. For example, ZnO quantum dot labeled immunosensor was prepared for CA 19-9 detection [12]. The immobilization process was performed by electrostatic forces based on ZnO' isoelectric point and a linearity of 0.1–180.0 U mL^{-1} with LOD of 0.04 U mL^{-1} was obtained. In addition, fluorescence immunoassay based on carbon quantum dots/AuNPs nanocomposite was developed and a linearity of 0.01–350.0 U mL^{-1} with LOD of 0.007 U mL^{-1} was obtained [13]. Finally, bimetallic CeO_2/FeO_x@mC_{500} based electrochemical immunosensor for sensitive detection of CA 19-9 was prepared. The antibody was incorporated to CeO_2/FeO_x@mC_{500} by chemical absorption and the immunosensor showed a low LOD of 10.0 μU mL^{-1} [3].

POMs as an inorganic compound have significant applications such as biochemistry [14] and sensor [15]. Especially, POMs can be used as reducing and stabilizing agents in aqueous solutions, suggesting the development of eco-friendly material synthesis [16]. Moreover, POMs' multi-electron redox ability provided the synthesis of noble metal nanoparticles [17,18]. Up to now, common UV irradiation method was applied to POM-incorporated metal NPs sysnthesis [19]. In addition, extra several approaches were presented for reduction of the metal precursor. Ultrasonication synthesis has attracted attention as scalable method for metal NPs sysnthesis, whereby the chemical effects of ultrasonic irradiation are tailored owing to the acoustic cavitation [20]. In this process, high temperature, pressure and cooling rates are significant conditions for metal NPs@POM [21].

Molybdenum sulfide (MoS_2) as layered transition metal dichalcogenide facilitates electron transfer owing to its abundant active edge sites [22]. Only few studies were presented about one-dimensional MoS_2 (1D-MoS_2) in comparison with two-dimensional MoS_2 for catalytic or photocatalytic applications [23]. For example, 1D-MoS_2 nanosheet incorporated $Ag_2Mo_2O_7$ microrods were prepared for catalytic oxidation of levofloxacin [24]. Recently, the excellent electrochemical performance of niobium was investigated [25]. Because of this, novel niobium based compounds were prepared [26,27]. Especially, niobium based oxides have been used frequently due to its improved electrochemical performances [28].

Herein, it was aimed to develop a novel sandwich-type electrochemical immunosensor based on 1D-MoS_2 nanorods/$LiNb_3O_8$ as signal amplification and polyoxometalate-incorporated gold nanoparticles as sensor platform to be utilized for CA 19-9 detection. Ultrasonication synthesis of AuNPs@POM nanocomposite was successfully performed and primer antibody immobilized to AuNPs@POM nanocomposite was conducted via amino-gold affinity. Then, 1D-MoS_2 NS/LNO was synthesized with high yield without waste formation. After the conjugation of seconder antibody to 1D-MoS_2 NS/LNO via π-π and electrostatic interactions, the sandwich-type electrochemical immunosensor was prepared by antibody-antigen interactions. Finally, electrochemical CA 19-9 immunosensor with fast, sensitive, environmentally friendly and low-cost suggests a pathway for clinical applications.

2. Experimental

2.1. Materials

CA 19-9, CA 19-9 primary antibody (anti-CA 19-9-Ab_1), CA 19-9 secondary antibody (anti-CA 19-9-Ab_2), carbohydrate antigen 24-2 (CA 242), carbohydrate antigen 125 (CA 125), prostate-specific antigen (PSA), bovine serum albumin (BSA), sodium molybdate dihydrate ($Na_2MoO_4{\cdot}2H_2O$), thioacetamide (CH_3CSNH_2), lithium hydroxide monohydrate ($LiOH{\cdot}H_2O$), niobium pentoxide (Nb_2O_5), polyoxometalate ($H_3PMo_{12}O_{40}$, POM), gold(III) chloride trihydrate ($HAuCl_4{\cdot}3H_2O$), sodium citrate ($Na_3C_6H_5O_7$) were purchased from Sigma-Aldrich. As supporting electrolyte and dilution buffer, 0.1 M phosphate-buffered saline (PBS) solution at pH of 7.0 was preferred.

2.2. Instruments

The surface morphologies of samples were investigated both by ZEISS EVO 50 SEM and JEOL 2100 TEM. The XRD patterns were recorded via Rigaku X-ray diffractometer using Cu-Kα radiation at λ = 0.154 nm. The XPS analysis was performend by PHI 5000 Versa Probe spectrometer. Furthermore, Gamry Reference 600 work-station (Gamry, USA) was used to perform electrochemical characterization techniques including CV, EIS and DPV.

2.3. Ultrasonication synthesis of AuNPs and AuNPs@POM nanocomposite

AuNPs was prepared by using $HAuCl_4{\cdot}3H_2O$ and $Na_3C_6H_5O_7$ as reducing agent according our previous paper [29].

The ultrasonic synthesis method was applied to the preparation of AuNPs@POM nanocomposite with mol ratio of AuNPs:POM (1:1) during 45 min. After the preparation of $HAuCl_4{\cdot}3H_2O$ aqueous solution (2.0 mM, 20.0 mL), $HAuCl_4{\cdot}3H_2O$ aqueous solution was tranferred into $H_3PMo_{12}O_{40}$ (POM) aqueous solution (2.0 mM, 40.0 mL) at 25 °C. After vigorous stirring, n-propanol (2.0 mL) was added into the dispersion. Then, the dispersion was transferred into Dewar cell (50.0 mL) and subjected to ultrasonication at acoustic power of 20 W. After sonoreaction, the colour of the solution converted into red, providing the formation of AuNPs. Thus, ***AuNPs@POM*** nanocomposite was stored at 25 °C [30].

2.4. AuNPs@POM/GCE as electrochemical sensor platform with anti-CA 19-9-Ab_1 and antigen CA 19-9 immobilizations

After the cleaning process of glassy carbon electrodes (GCEs) with 0.1 μm and 0.05 μm alumina slurries, respectively for 30 min, the alumina remains were eliminated by using acetonitrile and GCEs were dried at 25 °C under argon gas. After the dropping of AuNPs@POM dispersion (20.0 μL) on GCE, infrared heat lamp was applied to remove the solvent. Hence, GCE modified with AuNPs@POM electrode was tagged as ***AuNPs@POM/GCE***.

After 100.0 μU mL^{-1} anti-CA 19-9-Ab_1 dispersion (30.0 μL) was prepared in 0.1 M PBS (pH 7.0), the prepared primer antibody dispersion was dropped on AuNPs@POM/GCE and left at 37.0 °C for 25 min. ***anti-CA 19-9-Ab_1/AuNPs@POM/GCE*** was developed thanks to amino-gold affinity between primer antibody and AuNPs [31]. After that, BSA (2.0% w/v) was incubated on anti-CA 19-9-Ab_1/AuNPs@POM/GCE at 37.0 °C for 25 min to remove non-specific interactions (***BSA/anti-CA 19-9-Ab_1/AuNPs@POM/GCE)***. The CA 19-9 immobilizations were carried out on BSA/anti-CA 19-9-Ab_1/AuNPs@POM/GCE by dropping of each CA 19-9 with different concentration on electrode surfaces for 25 min at 37.0 °C and the antibody-antigen affinity provided CA 19-9/BSA/anti-CA 19-9-Ab_1/AuNPs@POM/GCE. Lastly, ***CA 19-9/BSA/anti-CA 19-9-Ab_1/AuNPs@POM/GCE*** was incubated in 0.1 M PBS (pH 7.0) to remove non-interacting antigen proteins.

2.5. Preparation of LNO, 1D-MoS_2 nanorods/$LiNb_3O_8$ (1D-MoS_2 NRs/LNO) and 1D-MoS_2 nanosheets/$LiNb_3O_8$ (1D-MoS_2 NS/LNO) composites

LNO powders were prepared by a calcination process. Nb_2O_5 (4.0 mmol) was dispered in $LiOH{\cdot}H_2O$ (40.0 mL) (the mole ratio of Li:Nb = 8:1) under vigirous stirring for 90 min. Then, the dispersion was transferred into a Teflon stainless autoclave at 200 °C for 20 h. After the centirifugation at 10000 rpm, the product was calcined from 400 to 850 °C for 90 min with a rate of 10 °C/min. After cooling up to 25 °C, ***LNO*** powders were collected.

$Na_2MoO_4{\cdot}2H_2O$ (25.0 mg) and CH_3CSNH_2 (15.0 mg) were dissolved in ultra-pure water (100.0 mL) under vigirous stirring. Then, the

dispersion was diluted with ultra-pure water to 50.0 mL. After the addition of LNO (75.0 mg) into this dispersion, the suspension was transferred into a Teflon stainless autoclave at 200 °C for 20 h. After the washing of the prepared material with ultra-pure water:ethanol (1:1), the product was dried at 50 °C under vacuum. Thus, 0.5 wt%1D-MoS_2 nanorods/LNO was tagged as ***0.5 wt%1D-MoS_2 NRs/LNO***. In addition, 1D-MoS_2 NRs/LNO including different amounts of 1D-MoS_2 (***1.0, 1.5, 2.0*** and ***2.5*** wt***% of 1D-MoS_2 NRs***) were prepared with the change of $Na_2MoO_4{\cdot}2H_2O$'s amount.

For 1D-MoS_2 NS preparation, $Na_2MoO_4{\cdot}2H_2O$ (0.50 g) and CH_3CSNH_2 (1.0 g) were firstly dissolved in ultra-pure water (100.0 mL) under vigirous stirring. Then, the suspension was transferred into a Teflon stainless autoclave at 200 °C for 20 h. After washing treatment, ***1D-MoS_2 NS*** powders were obtained. After that, 1D-MoS_2 NS powder (1.0 mg) and LNO (100.0 mg) were together grinded for 2 h in mortar including ethanol (1.0 mL). After ethanol evaporation, ***1.0 wt%1D-MoS_2 NS/LNO*** was prepared as a reference in comparison with 1D-MoS_2 NRs/LNO samples.

2.6. 1D-MoS_2 NRs/LNO as signal amplification with anti-CA 19-9-Ab_2 conjugation

After 100.0 μU mL^{-1} anti-CA 19-9-Ab_2 dispersion (30.0 μL) was prepared in 0.1 M PBS (pH 7.0), this dispersion was interacted with 1D-MoS_2 NRs/LNO (30.0 μL, 50.0 mg mL^{-1}) dispersion under magnetic stirring at 37.0 °C for 25 min. The centrifugation was performed at 5000

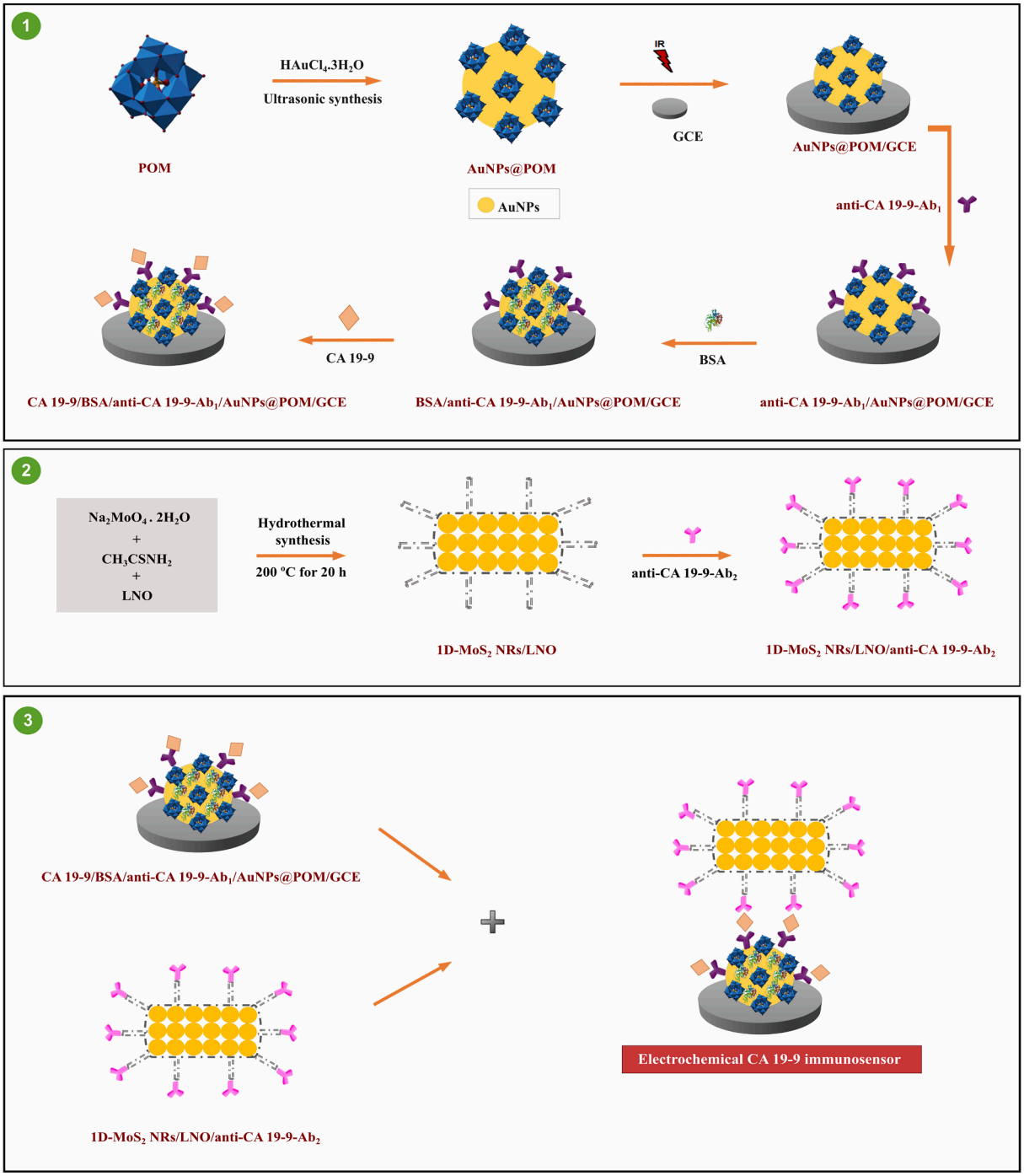

Scheme 1. Preparation procedure of electrochemical CA 19-9 immunosensor.

rpm during 20 min and the obtained ***1D-MoS_2 NRs/LNO/anti-CA 19-9-Ab_2*** was preserved in pH 7.0, 0.1 M PBS.

2.7. Electrochemical characterizations

The sandwich-type electrochemical immunosensor was prepared by antibody-antigen affinity between 1D-MoS_2 NRs/LNO/anti-CA 19-9-Ab_2 and CA 19-9/BSA/anti-CA 19-9-Ab_1/AuNPs@POM/GCE. 1D-MoS_2 NRs/LNO/anti-CA 19-9-Ab_2 dispersion (30.0 μL, 25.0 mg mL^{-1}) was dropped on CA 19-9/BSA/anti-CA 19-9-Ab_1/AuNPs@POM/GCE at 37.0 °C for the immune reaction time of 25 min. Thus, the developed sandwich-type electrochemical immunosensor was tagged as ***1D-MoS_2 NRs/LNO/anti-CA 19-9-Ab_2/CA 19-9/BSA/anti-CA 19-9-Ab_1/AuNPs@POM/GCE***. The prepared sandwich-type immunosensor for CA 19-9′s recognition was stored in pH 7.0, 0.1 M PBS (2.0 mL). 0.1 M PBS (pH 7.0, 2.0 mL) containing 1.0 mM H_2O_2 as a redox probe was used for electrochemical performance measurements. Differential pulse voltammograms (DPVs) were recorded at + 0.30 V in an enclosed cabinet. Briefly, the preparation procedures were shown on Scheme 1, including in 1D-MoS_2 NRs/LNO, AuNPs@POM/GCE, the immobilizations of proteins and the final electrochemical immunosensor development.

2.8. Sample preparation

CA 19-9 free plasma samples were supplied from Blood Bank in TURKEY. Sample preparation protocol was explained in detail on Supplemantary Data [5].

3. Results and discussion

3.1. Principle of electrochemical CA 19-9 immunosensor based on 1D-MoS_2 NRs/LNO and AuNPs@POM

In this study, 1D-MoS_2 NRs/LNO as signal amplification and AuNPs@POM as sensor platform/surface were prepared for immunosensor application. Especially, the sensor platform having high stability was developed owing to negative surface charge thanks to PMo_{12} polyanions on AuNPs. Thus, obvious electrostatic repulsions result in less coagulation, providing stable sensor surface development [32]. Another reason for this high stability was the formation of stable hydrogen bonding between hydroxyl groups on H_2O and PMo_{12} polyanions on AuNPs. In addition, there are two important factors corresponding to PMo_{12} polyanions' formation on AuNPs surface. (i) the increase of mass transfer because of acoustic shock waves and (ii) surface corrosion. Thus, the dominant factor can adjust PMo_{12} polyanions' formation on AuNPs. In generally, the first factor enables the formation of PMo_{12} polyanions, however, second factor determines the desorption of PMo_{12} polyanions from AuNPs surface. We can say that there is equal effect between the two factors in this study. Hence, AuNPs@POM as sensor platform/surface generally had two aims including the obtainment of the binding sites for primer antibody via amino-gold affinity and the increase of surface conductivity.

The porous LNO formation was corresponded to Li element's local enrichment, providing the connections of LNO particles [33]. Li enrichment area as LNO particles' junction site was composed of low formation energy, causing the direct growth of 1D-MoS_2 NRs. During direct growth of 1D-MoS_2 NRs, the incorporation of oxygen into sulfur sites on 1D-MoS_2 NRs and crystal defects occured as a result of lattice fringes (0.67 nm) of 1D-MoS_2 NRs in comparison with bulk MoS_2 (0.61 nm) [34,35]. After that, the easy incorporation of seconder CA 19-9 antibody was conducted by strong π-π and electrostatic interactions between seconder antibody and 1D-MoS_2 NRs [36].

H_2O_2 as a redox probe was used in electrochemical immunosensor application to monitor its conversion into O_2 at about + 0.30 V [31].

3.2. Characterizations of LNO, 1D-MoS_2 NRs/LNO and 1D-MoS_2 NS/LNO

Fig. 1 indicated XRD patterns of LNO and 1D-MoS_2 NRs/LNO including different amounts of 1D-MoS_2. According to Fig. 1, the characteristic diffraction peaks at 2Θ = 21.57°, 24.29°, 29.95°, 30.94°, 35.77°, 51.37° and 53.15° on the whole samples were corresponded to (011), (400), (410), (202), (212) and (14) crystalline planes of LNO, respectively. However, XRD patterns of 1D-MoS_2 NRs/LNO could not show the characteristic peaks of MoS_2 owing to low concentration of MoS_2 on LNO's surface [37,38]. Hence, HRTEM and XPS methods were used to show the presence of MoS_2 on the samples. Raman spectra (Fig. S1A) were obtained for LNO, pristine MoS_2 nanosheets (1D-MoS_2 NS), 1.0 wt%1D-MoS_2 NRs/LNO and 1.0 wt%1D-MoS_2 NS/LNO. Raman peaks at 381 and 404 cm^{-1} were corresponded to low-energy E^1_{2g} and high-energy A_{1g} modes of 2H-MoS_2 phase, respectively. In addition, the small peak at 335 cm^{-1} was attributed to photon mode (J_3) of metallic 1T-MoS_2 phase [39]. Thus, 1D-MoS_2 NS was composed of 1T and dominant 2H phases [39]. Nonetheless, after the preparation of 1.0 wt% 1D-MoS_2 NS/LNO, no evident MoS_2 phase was obtained for 1.0 wt%1D-MoS_2 NS/LNO such as 1.0 wt%1D-MoS_2 NRs/LNO with small MoS_2 loading. Furthermore, Raman peaks of LNO were overlapped with that of MoS_2. The characteristic layered structure of 1D-MoS_2 NS was also verified by SEM image (Fig. S1B).

Chemical states and surface compositions of 1.0 wt%1D-MoS_2 NRs/LNO were also shown by XPS measurements (Fig. S2). XPS survey demonstrated S2p, Nb3d, Mo3d and O1s peaks (Fig. S2A). Especially, XPS intensities of of Mo and S elements were low owing to the low amounts. In addition, the peaks at 210.1 and 206.8 eV (Fig. S2B) were corresponded to $Nb3d_{1/2}$ and $Nb3d_{3/2}$, respectively and the peaks at 530.2 and 532.3 eV (Fig. S2C) were attributed to Nb-O binding and non-lattice oxygen, respectively on XPS spectrum of O1s [40]. Finally, the peaks at 232.9 and 163.8 eV were attributed to Mo3d3/2 and S2p1/2 of MoS_2, respectively (Fig. S2D and Fig. S2E) [41]. Thus, the succesful preparation of 1.0 wt%1D-MoS_2 NRs/LNO with the presence of molybdenum, sülfür, niobium and oxygen elements was confirmed.

In addition, the morphological and microstructural properties of LNO and 1.0 wt%1D-MoS_2 NRs/LNO were investigated. According to Fig. 2A, LNO particles were aggregated to form a porous structure. Then, 1D-MoS_2 NRs was grown on junction sites of LNO particles (Fig. 2B and light blue circles on Fig. 2C). The average sizes of 1D-MoS_2 NRs changed from several nanometers to 50 nm and the length of 1D-MoS_2 NRs changed from 100 nm to 220 nm (Fig. 2D). According to HRTEM image

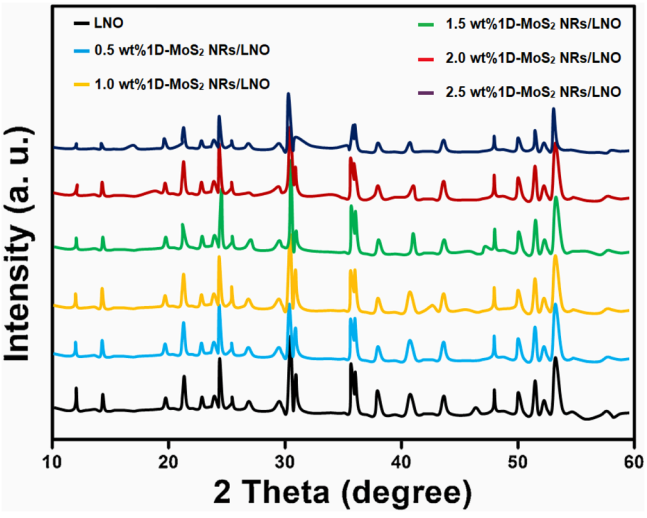

Fig. 1. XRD patterns of LNO and 1D-MoS_2 NRs/LNO including different amounts of 1D-MoS_2.

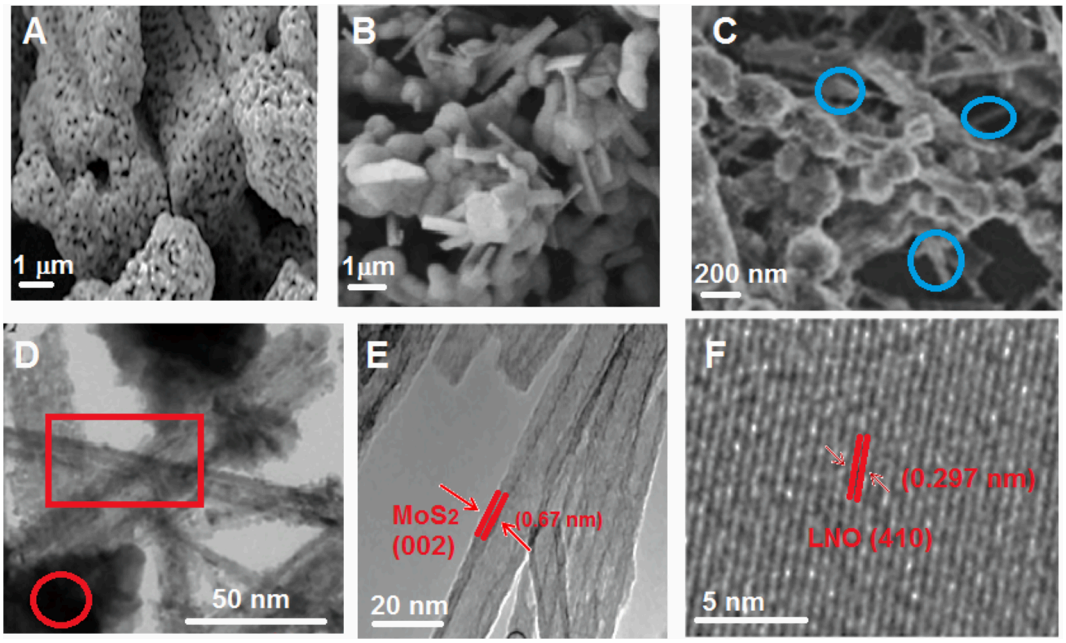

Fig. 2. SEM images of (A) LNO powder, (B) and (C) 1.0 wt%1D-MoS_2 NRs/LNO, TEM image of (D) 1.0 wt%1D-MoS_2 NRs/LNO and HRTEM images of (E) and (F) 1.0 wt%1D-MoS_2 NRs/LNO.

of 1.0 wt%1D-MoS_2 NRs/LNO (Fig. 2E), the lattice fringes of 1D-MoS_2 NRs was evaluated as 0.67 nm, indicating (002) plane of hexagonal MoS_2. Finally, the interplanar spacing (0.297 nm) of LNO particle was attributed to *d*-spacing of (410) crystal plane (Fig. 2F) [42].

UV–vis spectroscopy (Fig. S3A) was utilized to evaluate the optical properties of the prepared samples. LNO showed an absorption band below 400 nm and the absorption increased with loading with 1D-MoS_2 NRs. According to these results, 1D-MoS_2 NRs/LNO can increase absorption ability with increase of 1D-MoS_2 NRs amount. In addition, PL spectra of LNO and 1.0 wt%1D-MoS_2 NRs/LNO were recorded at 250 nm excitation (Fig. S3B). LNO having high recombination of photogenerated charges showed the highest emission. However, the emission was quenched on 1.0 wt%1D-MoS_2 NRs/LNO, suggesting the easy electron transfer from LNO to 1D-MoS_2 NRs. Thus, this easy electron transfer could provide the enhancement of catalytic activity.

3.3. Characterizations of AuNPs@POM composite

XRD pattern (Fig. 3A) of AuNPs@POM composite demonstrated face-centered cubic structure of metallic gold nanoparticles and the peaks at 37.93°, 44.28°, 64.47° and 77.68° were corresponded to (111), (200), (220) and (311) planes [43,44]. According to Fig. 3A, the peak attributing to (111) plane was sharper than that of the other planes, suggesting predominant orientation of Au (111). In addition, the absence of XRD peaks corresponding to POM means the adsorption of POM on AuNPs surface without agglomeration [45]. FTIR spectra (Fig. 3B) were recorded to confirm the presence of AuNPs@POM composite. The absorption bands at 1065 cm^{-1} and 965 cm^{-1} were resulted from P–O and Mo–O_d groups of pure polyoxometalate whereas these absorption peaks were observed on longer wavelengths at 1090 cm^{-1} and 1022 cm^{-1} on FTIR spectrum of AuNPs@POM composite. This situation showed the obvious interaction between POM and gold nanoparticles. The vibration peak at 880 cm^{-1} corresponding to Mo–O_b–Mo group on FTIR spectrum of POM disappeared on AuNPs@POM composite [46]. In addition, the vibration peak at 800 cm^{-1} attributing to Mo–O_c–Mo group on POM was observed at 620 cm^{-1} on AuNPs@POM composite. Finally, the succesful synthesis of AuNPs@POM composite was confirmed by FTIR measurements.

Cyclic voltammograms (Fig. S4) were recorded for the electrochemical comparison of POM and AuNPs@POM composite. According to Fig. S4, a multi-electron reversible redox reaction was observed in DMF solution containing 1.0 M H_2SO_4. The electrochemical peaks at −0.02, +0.16 and + 0.38 V were corresponded to POM's redox behavior. Hence, the successful adsorption of POM on AuNPs surface without agglomeration was verified by CV.

Finally, TEM and SEM measurements were performed for

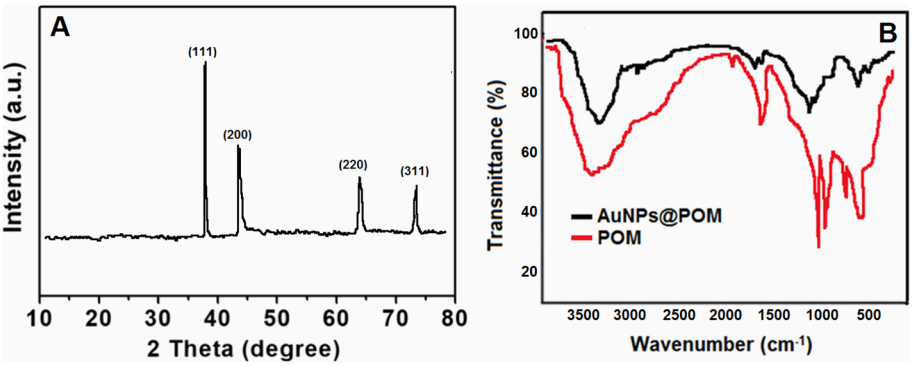

Fig. 3. (A) XRD pattern of AuNPs@POM composite and (B) FTIR spectra of POM and AuNPs@POM composite.

AuNPs@POM composite. According to Fig. 4A, irregular AuNPs on POM had a narrow size distribution. The average particle diameters of AuNPs were obtained as about 30–35 nm and the whole AuNPs was well dispersed owing to electrostatic repulsion thanks to PMo_{12} polyanions on AuNPs. In addition, Fig. 4B showed the uniform distribution of AuNPs in two-dimensional monolayer manner.

3.4. Electrochemical characterizations of sensor platform and signal amplification

First of all, CV measurements (Fig. 5A) were conducted in 1.0 mM $[Fe(CN)_6]^{3-}$ solution containing 0.1 M KCl to characterize the sensor plaform. The unmodified GCE demonstrated small anodic and cathodic electrochemical signals (curve a). Due to AuNPs' optical properties, a large surface area and electrical conductivity [47,48], the increase on electrochemical signals was observed (curve b). Lastly, more electrochemical signals were observed because of POMs' multi-electron redox ability and synergistic effect between POM and AuNPs (curve c) [30]. Then, the immobilizations of anti-CA 19-9-Ab_1, BSA and CA 19-9 on AuNPs@POM/GCE decreased the electrochemical immunosensor's performance owing to electron transfer blocking (curve d, curve e and curve f). Hence, the incubations of primer antibody, BSA and CA 19-9 on immunosensor platform were succesfully conducted.

In addition, EIS measurements (Fig. 5B) were conducted by using different electrochemical sensor platform as CV measurements. According to EIS graphs of AuNPs/GCE (curve b) and AuNPs@POM/GCE (curve c), mass transfer resistances on the electrode surface decreased when bare GCE (curve a) was modified with AuNPs and AuNPs@POM. As in the CV experiments, when primer antibody (curve d), BSA (curve e) and CA 19-9 (curve f) were immobilized to the sensor platform, the electron transfer rate decreased.

EIS graphs (Fig. 5C) of various immunosensors including different signal amplification such as (a) LNO, (b) 1.0 wt%1D-MoS_2 NS/LNO and (c) 1.0 wt%1D-MoS_2 NRs/LNO were obtained. Thus, electron transfer rate at 1.0 wt%1D-MoS_2 NS/LNO was faster than that of LNO owing to 1.0 wt%1D-MoS_2 NS' abundant active edge sites [22]. Due to the direct growth of 1D-MoS_2 NRs on LNO, 1.0 wt%1D-MoS_2 NRs/LNO (curve c) facilitated the electron transfer from LNO to 1D-MoS_2 NRs in short distance in comparison with curve b. In addition, because of efficient separation of electrons and contact interface between LNO and 1D-MoS_2 NRs, the electrochemical activity for CA 19-9 detection increased.

Finally, DPV responses of various immunosensors based on 1D-MoS_2 NRs/LNO including different amounts of 1D-MoS_2 were recorded. According to Fig. 5D, the electrochemical currents increased with the amounts of 1D-MoS_2 NRs. Hence, as expected, the highest electrochemical currents were observed by using CA 19-9 electrochemical immunosensor based on 2.5 wt%1D-MoS_2 NRs/LNO. AuNPs@POM/GCE as electrochemical sensor platform and 2.5 wt%1D-MoS_2 NRs/LNO as signal amplification were used for subsequent immunosensor applications.

3.5. Optimization for electrochemical measurements

Detailed investigation was implemented for lighting up the effect of pH, immune reaction time, H_2O_2 and 2.5 wt%1D-MoS_2 NRs/LNO/anti-CA 19-9-Ab_2 solution concentration (Fig. S5).

3.6. Linearity range

The sensitivity and linearity range studies of the prepared immunosensor for CA 19-9 analysis were evaluated. According to Fig. 6, the electrochemical currents increased with CA 19-9 amounts. The calibration plot demonstrated a linearity between immunosensor responses and CA 19-9 concentration in the range of 0.10–10.0 μU mL^{-1} (R^2 = 0.9989). The regression equation was obtained as y (I, μA) = 0.4725x (CA 19-9 concentration, μU mL^{-1}) + 0.0089 (inset of Fig. 6). The quantification limit (LOQ) and LOD values were obtained as 0.10 μU mL^{-1} and 0.030 μU mL^{-1}, respectively, by the Eqs. (1) and (2):

$$LOQ = 10.0\ S/m \quad (1)$$

$$LOD = 3.3\ S/m \quad (2)$$

where S is the standard deviation of the intercept and m is the slope of the regression line. Table 1 showed the comparison features between the prepared immunosensor and the other analytical methods. Owing to 1D-MoS_2 NRs' active sites and porous LNO's high surface area, LOD of the prepared immunosensor for CA 19-9 demonstrated a relatively low detection limit in comparison with the other materials/methods. Furthermore, the ultrasonic synthesis of AuNPs@POM nanocomposite and the hydrothermal synthesis of 1D-MoS_2 NRs/LNO caused little waste generation, suggesting environmentally friendly immunosensor construction. Hence, this CA 19-9 immunosensor has potential practical applications for early diagnosis.

3.7. Recovery

Recovery values of CA 19-9 in the presence of 0.1 M PBS (pH 7.0) containing 1.0 mM H_2O_2 were listed on Table S1. These values were calculated by the Eq. (3) below:

$$\boldsymbol{Recovery = Found\ CA\ 19-9,\ \mu U\ mL^{-1} / Real\ CA\ 19-9,\ \mu U\ mL^{-1}} \quad (3)$$

According to Table S1, the close values to 100.00% showed that potential interferences had no important effects on CA 19-9 detection by the prepared immunosensor. In addition, the standard addition method (SAM) was applied the plasma samples and the calibration equation of SAM was obtained as y (I, μA) = 0.4794x (CA 19-9 concentration, μU

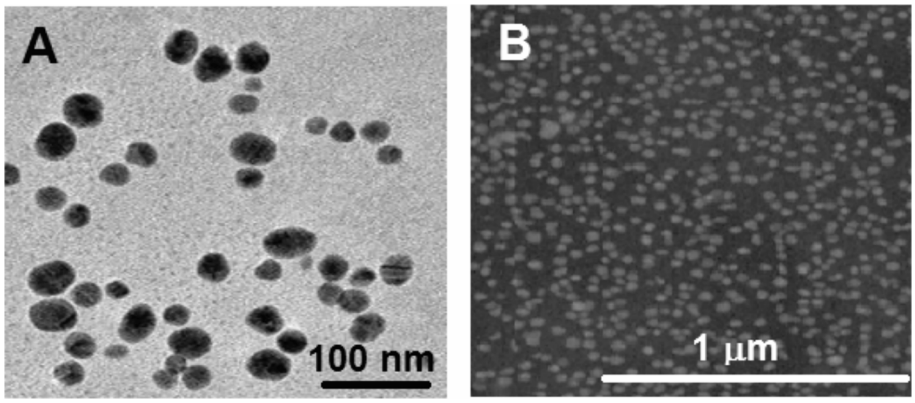

Fig. 4. (A) TEM and (B) SEM images of AuNPs@POM composite.

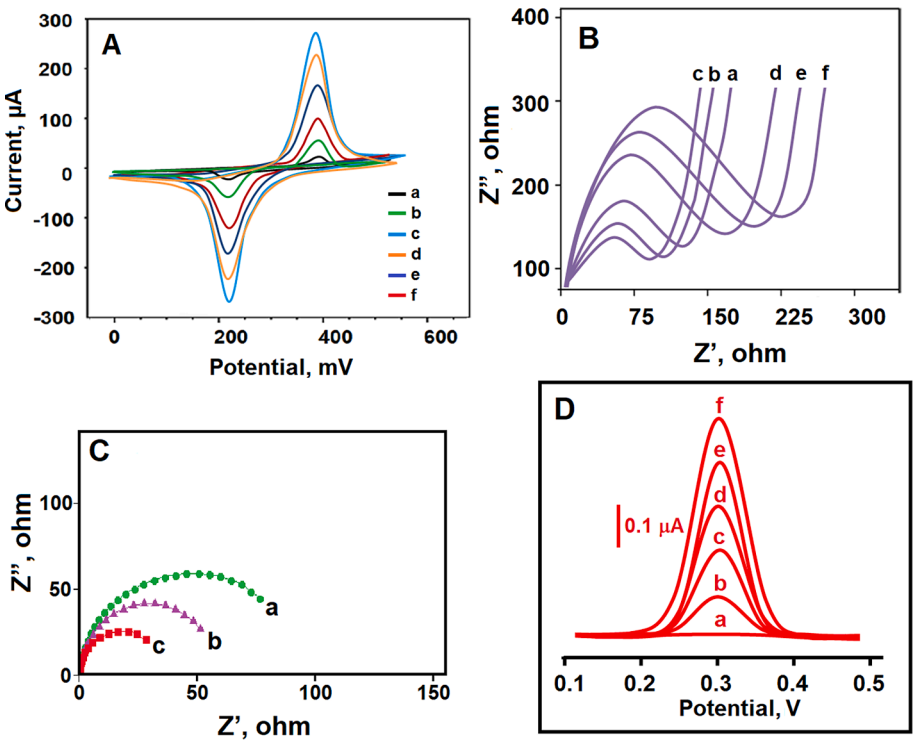

Fig. 5. (A) Cyclic voltammograms, (B) EIS graphs at (a) bare GCE, (b) AuNPs/GCE, (c) AuNPs@POM/GCE, (d) anti-CA 19-9-Ab_1/AuNPs@POM/GCE, (e) BSA/anti-CA 19-9-Ab_1/AuNPs@POM/GCE, (f) CA 19-9/BSA/anti-CA 19-9-Ab_1/AuNPs@POM/GCE (scan rate of 50 mV s^{-1}) in 1.0 mM $[Fe(CN)_6]^{3-}$ containing 0.1 M KCl, (C) EIS graphs of various immunosensors including different signal amplification such as (a) LNO, (b) 1.0 wt%1D-MoS_2 NS/LNO and (c) 1.0 wt% 1D-MoS_2 NRs/LNO) in 1.0 mM $[Fe(CN)_6]^{3-}$ containing 0.1 M KCl (the presence of 1.0 µU mL^{-1} CA 19-9), (D) DPV responses of various immunosensors including different signal amplification such as (b) 0.5 wt%1D-MoS_2 NRs/LNO, (c) 1.0 wt%1D-MoS_2 NRs/LNO, (d) 1.5 wt%1D-MoS_2 NRs/LNO, (e) 2.0 wt %1D-MoS_2 NRs/LNO and (f) 2.5 wt%1D-MoS_2 NRs/LNO in absence of H_2O_2 (curve a) and in presence of 1.0 mM H_2O_2 (the presence of 1.0 µU mL^{-1} CA 19-9).

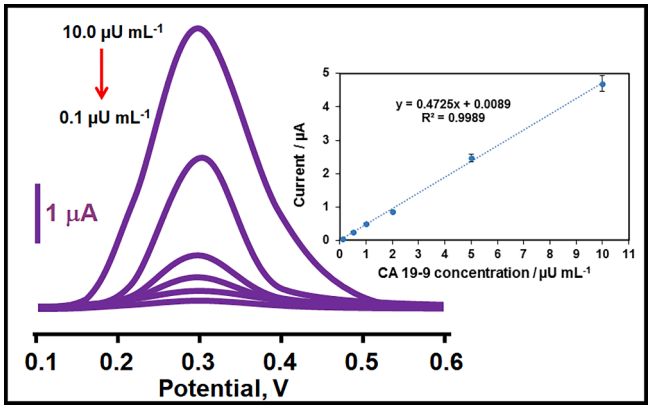

Fig. 6. Concentration effect (from 0.10 to 10.0 µU mL^{-1} CA 19-9) on immunosensor signals, Inset: Calibration curve for electrochemical CA 19-9 immunosensor.

Table 1
The comparison of electrochemical CA 19-9 immunosensor with other reported techniques.

Material/Method	Linear Range	LOD	Ref.
Au@Pd-Gra/Thi	0.015–150.0 U mL^{-1}	0.006 U mL^{-1}	[49]
PDA-Ag NPs	0.0001–100.0 U mL^{-1}	0.000032 U mL^{-1}	[50]
nanoFe_3O_4@GO	0.001–5.0 U mL^{-1}	0.0005 U mL^{-1}	[1]
CNOs/GO	0.3–100.0 U mL^{-1}	0.12 U mL^{-1}	[51]
TiO_2NWs/Au/CdSe@ZnS	0.01–200 U mL^{-1}	0.0039 U mL^{-1}	[4]
AgNPs@ZIF-67	0.0001–10 U mL^{-1}	31.0 µU mL^{-1}	[52]
CQDs/Au	0.01–350 U mL^{-1}	0.0070 U mL^{-1}	[13]
CeO_2/FeO_x@mC_{500}	0.0001–10.0 U mL^{-1}	10.0 µU mL^{-1}	[3]
Sandwich type immunosensor	***0.1–10.0 µU mL^{-1}***	***0.030 µU mL^{-1}***	***This study***

mL^{-1}) + 0.1073. Especially, the close slopes between SAM and linear regression method confirmed successful analysis of CA 19-9 without the effect of other agents.

3.8. Selectivity, stability and reusability

For selectivity studies (Fig. S6A) of electrochemical CA 19-9 immunosensor, five solution mixtures were separately prepared such as (i) 1.0 µU mL^{-1} CA 19-9, (ii) 1.0 µU mL^{-1} CA 19-9 + 10.0 µU mL^{-1} CA 242, (iii) 1.0 µU mL^{-1} CA 19-9 + 10.0 µU mL^{-1} CA 125, (iv) 1.0 µU mL^{-1} CA 19-9 + 10.0 µU mL^{-1} PSA, (v) 1.0 µU mL^{-1} CA 19-9 + 10.0 µU mL^{-1} BSA. Then, the five electrochemical CA 19-9 immunosensors were separately prepared by using these solution mixtures. After that, these five electrochemical CA 19-9 immunosensors were applied to 1.0 mM H_2O_2 solution including in pH 7.0, 0.1 M PBS (2.0 mL) and 0.38% of relative standard deviation (RSD) was obtained, providing the high selectivity of electrochemical CA 19-9 immunosensor.

The stability tests (Fig. S6B) of electrochemical CA 19-9 immunosensor were performed at 25.0 °C during 6 weeks in the presence of 1.0 mM H_2O_2. According to Fig. S6B, the electrochemical current values were about 98.83% of first current signal and 0.81% of RSD for current signals was observed. Thereby, stable CA 19-9 immunosensor can be applied for clinical samples for a long time.

Finally, reusability of electrochemical CA 19-9 immunosensor was evaluated in 1.0 mM H_2O_2 solution (Fig. S6C). 0.18% of RSD for current signals was obtained during 50 times usage of electrochemical CA 19-9 immunosensor. Hence, high reusability of electrochemical CA 19-9 immunosensor can be mentioned for subsequent clinical applications.

4. Conclusions

In conclusion, a novel electrochemical immunosensor based on 1D-MoS_2 nanorods/$LiNb_3O_8$ and AuNPs@POM was presented for carbohydrate antigen 19-9 (CA 19-9) detection. This developed immunosensor has some advantages such as simplicity, fast analysis, high selectivity, stability, accuracy and precision and showed a low sensitivity (LOD of 0.030 µU mL^{-1}). In addition, the close recovery values to

100.00% in plasma samples provided a important bioanalytical method development for CA 19-9 determination. Hence, this study firstly indicated the application of a novel immunosensor for cancer disease diagnosis. Furthermore, low-cost and environmentally friendly immunosensor was prepared as an alternative detection method for the determination of malignant tumors.

CRediT authorship contribution statement

Mehmet Lütfi Yola: Supervision, Conceptualization, Writing - review & editing. **Necip Atar:** Data curation, Writing - original draft, Visualization, Investigation.

Declaration of Competing Interest

The authors declare that they have no known competing financial interests or personal relationships that could have appeared to influence the work reported in this paper.

Acknowledgement

Mehmet Lütfi YOLA would like to thank Turkish Academy of Sciences for their invaluable support in respect to The Young Scientists Award Programme, TÜBA-GEBIP (2019). The study was partially supported with this award.

Appendix A. Supplementary data

Supplementary data to this article can be found online at https://doi.org/10.1016/j.microc.2021.106643.

References

[1] Y. Sha, Z. Guo, B. Chen, S. Wang, G. Ge, B. Qiu, X. Jiang, A one-step electrochemiluminescence immunosensor preparation for ultrasensitive detection of carbohydrate antigen 19-9 based on multi-functionalized graphene oxide, Biosens. Bioelectron. 66 (2015) 468–473.
[2] B.F. Atkinson, C.S. Ernst, M. Herlyn, Z. Steplewski, H.F. Sears, H. Koprowski, Gastrointestinal cancer-associated antigen in immunoperoxidase assay, Cancer Res. 42 (1982) 4820.
[3] M. Wang, M. Hu, B. Hu, C. Guo, Y. Song, Q. Jia, L. He, Z. Zhang, S. Fang, Bimetallic cerium and ferric oxides nanoparticles embedded within mesoporous carbon matrix: electrochemical immunosensor for sensitive detection of carbohydrate antigen 19-9, Biosens. Bioelectron. 135 (2019) 22–29.
[4] H. Zhu, G.-C. Fan, E.S. Abdel-Halim, J.-R. Zhang, J.-J. Zhu, Ultrasensitive photoelectrochemical immunoassay for CA19-9 detection based on CdSe@ZnS quantum dots sensitized TiO_2NWs/Au hybrid structure amplified by quenching effect of Ab2@V2+ conjugates, Biosens. Bioelectron. 77 (2016) 339–346.
[5] M.L. Yola, N. Atar, Development of cardiac troponin-I biosensor based on boron nitride quantum dots including molecularly imprinted polymer, Biosens. Bioelectron. 126 (2019) 418–424.
[6] H. Karimi-Maleh, O.A. Arotiba, Simultaneous determination of cholesterol, ascorbic acid and uric acid as three essential biological compounds at a carbon paste electrode modified with copper oxide decorated reduced graphene oxide nanocomposite and ionic liquid, J. Colloid Interface Sci. 560 (2020) 208–212.
[7] H. Karimi-Maleh, F. Karimi, M. Alizadeh, A.L. Sanati, Electrochemical sensors, a bright future in the fabrication of portable kits in analytical systems, Chem. Rec. 20 (2020) 682–692.
[8] A. Khodadadi, E. Faghih-Mirzaei, H. Karimi-Maleh, A. Abbaspourrad, S. Agarwal, V.K. Gupta, A new epirubicin biosensor based on amplifying DNA interactions with polypyrrole and nitrogen-doped reduced graphene: experimental and docking theoretical investigations, Sens. Actuators, B 284 (2019) 568–574.
[9] H. Karimi-Maleh, M. Sheikhshoaie, I. Sheikhshoaie, M. Ranjbar, J. Alizadeh, N. W. Maxakato, A. Abbaspourrad, A novel electrochemical epinine sensor using amplified CuO nanoparticles and a n-hexyl-3-methylimidazolium hexafluorophosphate electrode, New J. Chem. 43 (2019) 2362–2367.
[10] H. Karimi-Maleh, M.L. Yola, N. Atar, Y. Orooji, F. Karimi, P. Senthil Kumar, J. Rouhi, M. Baghayeri, A novel detection method for organophosphorus insecticide fenamiphos: molecularly imprinted electrochemical sensor based on core-shell Co_3O_4@MOF-74 nanocomposite, J. Colloid Interface Sci. 592 (2021) 174–185.
[11] M.L. Yola, N. Atar, N. Özcan, A novel electrochemical lung cancer biomarker cytokeratin 19 fragment antigen 21-1 immunosensor based on Si3N4/MoS2 incorporated MWCNTs and core–shell type magnetic nanoparticles, Nanoscale 13 (2021) 4660–4669.
[12] B. Gu, C. Xu, C. Yang, S. Liu, M. Wang, ZnO quantum dot labeled immunosensor for carbohydrate antigen 19-9, Biosens. Bioelectron. 26 (2011) 2720–2723.
[13] N.A. Alarfaj, M.F. El-Tohamy, H.F. Oraby, CA 19-9 Pancreatic tumor marker fluorescence immunosensing detection via immobilized carbon quantum dots conjugated gold nanocomposite, Int. J. Mol. Sci. 19 (2018) 1162.
[14] H.G.T. Ly, G. Absillis, R. Janssens, P. Proost, T.N. Parac-Vogt, Highly amino acid selective hydrolysis of myoglobin at aspartate residues as promoted by Zirconium (IV)-substituted polyoxometalates, Angew. Chem. Int. Ed. 54 (2015) 7391–7394.
[15] A. González, N. Gálvez, M. Clemente-León, J.M. Dominguez-Vera, Electrochromic polyoxometalate material as a sensor of bacterial activity, Chem. Commun. 51 (2015) 10119–10122.
[16] D.-F. Chai, Z. Ma, H. Yan, Y. Qiu, H. Liu, H.-D. Guo, G.-G. Gao, Synergistic effect of sandwich polyoxometalates and copper–imidazole complexes for enhancing the peroxidase-like activity, RSC Adv. 5 (2015) 78771–78779.
[17] M.L. Yola, V.K. Gupta, N. Atar, New molecular imprinted voltammetric sensor for determination of ochratoxin A, Mater. Sci. Eng. C 61 (2016) 368–375.
[18] N. Atar, M.L. Yola, T. Eren, Sensitive determination of citrinin based on molecular imprinted electrochemical sensor, Appl. Surf. Sci. 362 (2016) 315–322.
[19] A. Ayati, A. Ahmadpour, F.F. Bamoharram, M.M. Heravi, H. Rashidi, Photocatalytic synthesis of gold nanoparticles using preyssler acid and their photocatalytic activity, Chin. J. Catal. 32 (2011) 978–982.
[20] H. Xu, K.S. Suslick, Sonochemical synthesis of highly fluorescent Ag nanoclusters, ACS Nano 4 (2010) 3209–3214.
[21] T.R. Bastami, M.H. Entezari, Synthesis of manganese oxide nanocrystal by ultrasonic bath: effect of external magnetic field, Ultrason. Sonochem. 19 (2012) 830–840.
[22] D. Voiry, R. Fullon, J. Yang, C. de Carvalho Castro e Silva, R. Kappera, I. Bozkurt, D. Kaplan, M.J. Lagos, P.E. Batson, G. Gupta, A.D. Mohite, L. Dong, D. Er, V. B. Shenoy, T. Asefa, M. Chhowalla, The role of electronic coupling between substrate and 2D MoS_2 nanosheets in electrocatalytic production of hydrogen, Nat. Mater. 15 (2016) 1003–1009.
[23] P. Li, H. Hu, J. Xu, H. Jing, H. Peng, J. Lu, C. Wu, S. Ai, New insights into the photo-enhanced electrocatalytic reduction of carbon dioxide on MoS_2-rods/TiO_2 NTs with unmatched energy band, Appl. Catal. B 147 (2014) 912–919.
[24] S. Adhikari, S. Mandal, D.-H. Kim, Z-scheme 2D/1D MoS_2 nanosheet-decorated $Ag_2Mo_2O_7$ microrods for efficient catalytic oxidation of levofloxacin, Chem. Eng. J. 373 (2019) 31–43.
[25] V. Augustyn, J. Come, M.A. Lowe, J.W. Kim, P.-L. Taberna, S.H. Tolbert, H. D. Abruña, P. Simon, B. Dunn, High-rate electrochemical energy storage through Li^+ intercalation pseudocapacitance, Nat. Mater. 12 (2013) 518–522.
[26] M.A. Reddy, U.V. Varadaraju, Lithium insertion into niobates with columbite-type structure: interplay between structure-composition and crystallite size, J. Phys. Chem. C 115 (2011) 25121–25124.
[27] H. Xu, J. Shu, X. Hu, Y. Sun, W. Luo, Y. Huang, Electrospun porous $LiNb_3O_8$ nanofibers with enhanced lithium-storage properties, J. Mater. Chem. A 1 (2013) 15053–15059.
[28] H. Zhai, H. Liu, H. Li, L. Zheng, C. Hu, X. Zhang, Q. Li, J. Yang, Hydrothermal-assisted sintering strategy towards porous- and hollow-structured $LiNb_3O_8$ anode material, Nanoscale Res. Lett. 12 (2017) 463.
[29] M.L. Yola, N. Atar, A novel voltammetric sensor based on gold nanoparticles involved in p-aminothiophenol functionalized multi-walled carbon nanotubes: application to the simultaneous determination of quercetin and rutin, Electrochim. Acta 119 (2014) 24–31.
[30] T.R. Bastami, A. Ghaedi, S.G. Mitchell, A. Javadian-Saraf, M. Karimi, Sonochemical synthesis of polyoxometalate-stabilized gold nanoparticles for point-of-care determination of acetaminophen levels: preclinical study in an animal model, RSC Adv. 10 (2020) 16805–16816.
[31] H. Medetalibeyoglu, M. Beytur, O. Akyıldırım, N. Atar, M.L. Yola, Validated electrochemical immunosensor for ultra-sensitive procalcitonin detection: carbon electrode modified with gold nanoparticles functionalized sulfur doped MXene as sensor platform and carboxylated graphitic carbon nitride as signal amplification, Sens. Actuators, B 319 (2020), 128195.
[32] T.R. Bastami, M.H. Entezari, High stable suspension of magnetite nanoparticles in ethanol by using sono-synthesized nanomagnetite in polyol medium, Mater. Res. Bull. 48 (2013) 3149–3156.
[33] H. Zhai, J. Qi, X. Zhang, H. Li, L. Yang, C. Hu, H. Liu, J. Yang, Preparation and photocatalytic performance of hollow structure $LiNb_3O_8$ photocatalysts, Nanoscale Res. Lett. 12 (2017) 519.
[34] X. Li, T. Li, Y. Ma, Q. Wei, W. Qiu, H. Guo, X. Shi, P. Zhang, A.M. Asiri, L. Chen, B. Tang, X. Sun, Boosted electrocatalytic N_2 reduction to NH_3 by defect-rich MoS_2 nanoflower, Adv. Energy Mater. 8 (2018) 1801357.
[35] X.-H. Zhang, N. Li, J. Wu, Y.-Z. Zheng, X. Tao, Defect-rich O-incorporated 1T-MoS_2 nanosheets for remarkably enhanced visible-light photocatalytic H_2 evolution over CdS: the impact of enriched defects, Appl. Catal. B 229 (2018) 227–236.
[36] J. Lu, J.H. Lu, H. Liu, B.o. Liu, L. Gong, E.S. Tok, K.P. Loh, C.H. Sow, Microlandscaping of Au nanoparticles on few-layer MoS_2 films for chemical sensing, Small 11 (2015) 1792–1800.
[37] X. Hu, S. Lu, J. Tian, N.a. Wei, X. Song, X. Wang, H. Cui, The selective deposition of MoS_2 nanosheets onto (101) facets of TiO_2 nanosheets with exposed (001) facets and their enhanced photocatalytic H_2 production, Appl. Catal. B 241 (2019) 329–337.
[38] Y.-J. Yuan, Z.-J. Ye, H.-W. Lu, B. Hu, Y.-H. Li, D.-Q. Chen, J.-S. Zhong, Z.-T. Yu, Z.-G. Zou, Constructing anatase TiO_2 nanosheets with exposed (001) facets/layered MoS_2 two-dimensional nanojunctions for enhanced solar hydrogen generation, ACS Catal. 6 (2016) 532–541.

[39] H.-Y. He, Z. He, Q. Shen, Efficient hydrogen evolution catalytic activity of graphene/metallic MoS_2 nanosheet heterostructures synthesized by a one-step hydrothermal process, Int. J. Hydrogen Energy 43 (2018) 21835–21843.
[40] H. Zhai, J. Kong, J. Yang, J. Xu, Q. Xu, H. Sun, A. Li, D.i. Wu, Resistive switching properties and failure behaviors of (Pt, Cu)/Amorphous ZrO_2/Pt sandwich structures, J. Mater. Sci. Technol. 32 (2016) 676–680.
[41] J. Hu, D. Chen, N. Li, Q. Xu, H. Li, J. He, J. Lu, In situ fabrication of $Bi_2O_2CO_3$/MoS_2 on carbon nanofibers for efficient photocatalytic removal of NO under visible-light irradiation, Appl. Catal. B 217 (2017) 224–231.
[42] Z. Jian, X. Lu, Z. Fang, Y.-S. Hu, J. Zhou, W. Chen, L. Chen, $LiNb_3O_8$ as a novel anode material for lithium-ion batteries, Electrochem. Commun. 13 (2011) 1127–1130.
[43] Z. Li, A. Friedrich, A. Taubert, Gold microcrystal synthesis via reduction of $HAuCl_4$ by cellulose in the ionic liquid 1-butyl-3-methyl imidazolium chloride, J. Mater. Chem. 18 (2008) 1008–1014.
[44] J. Xu, T. Zhao, Z. Liang, L. Zhu, Facile preparation of AuPt alloy nanoparticles from organometallic complex precursor, Chem. Mater. 20 (2008) 1688–1690.
[45] S. Khadempir, A. Ahmadpour, M.T. Hamed Mosavian, N. Ashraf, F.F. Bamoharram, R. Fernández-Pacheco, J.M. de la Fuente, S.G. Mitchell, Mechanistic insights into the activation process in electrocatalytic ethanol oxidation by phosphomolybdic acid-stabilised palladium(0) nanoparticles (PdNPs@PMo_{12}), RSC Adv. 6 (2016) 5359–5366.
[46] S. Khadempir, A. Ahmadpour, M.T. Hamed Mosavian, N. Ashraf, F.F. Bamoharram, S.G. Mitchell, J.M. de la Fuente, A polyoxometalate-assisted approach for synthesis of Pd nanoparticles on graphene nanosheets: synergistic behaviour for enhanced electrocatalytic activity, RSC Adv. 5 (2015) 24319–24326.
[47] E.C. Dreaden, L.A. Austin, M.A. Mackey, M.A. El-Sayed, Size matters: gold nanoparticles in targeted cancer drug delivery, Ther. Deliv. 3 (2012) 457–478.
[48] P. Singh, S. Pandit, V.R.S.S. Mokkapati, A. Garg, V. Ravikumar, I. Mijakovic, Gold nanoparticles in diagnostics and therapeutics for human cancer, Int. J. Mol. Sci. 19 (2018) 1979.
[49] W. Li, D. Shu, D. Zhang, Z. Ma, Multi-amplification of the signal of voltammetric immunosensors: Highly sensitive detection of tumor marker, Sens. Actuators, B 262 (2018) 50–56.
[50] N. Zhang, D. Zhang, C. Chu, Z. Ma, Label-assisted chemical adsorption triggered conversion of electroactivity of sensing interface to achieve the Ag/AgCl process for ultrasensitive detection of CA 19-9, Anal. Chim. Acta 1093 (2020) 43–51.
[51] G. Ibáñez-Redín, R.H.M. Furuta, D. Wilson, F.M. Shimizu, E.M. Materon, L.M.R. B. Arantes, M.E. Melendez, A.L. Carvalho, R.M. Reis, M.N. Chaur, D. Gonçalves, O. N. Oliveira Jr, Screen-printed interdigitated electrodes modified with nanostructured carbon nano-onion films for detecting the cancer biomarker CA19-9, Mater. Sci. Eng. C 99 (2019) 1502–1508.
[52] G. Mo, X. He, D. Qin, S. Meng, Y. Wu, B. Deng, Spatially-resolved dual-potential sandwich electrochemiluminescence immunosensor for the simultaneous determination of carbohydrate antigen 19-9 and carbohydrate antigen 24–2, Biosens. Bioelectron. 178 (2021), 113024.